Next Energy 4 (2024) 100136

Contents lists available at ScienceDirect

Next Energy

journal homepage: www.sciencedirect.com/journal/next-energy

Research article

Stabilizing high temperature operation and calendar life of $LiNi_{0.5}Mn_{1.5}O_4$

Weiliang Yao[a,1], Yixuan Li[b,1], Marco Olguin[b,c,1], Shuang Bai[a], Marshall A. Schroeder[e], Weikang Li[b], Alex Liu[b], Na Ri Park[b], Bhargav Bhamwala[b], Baharak Sayahpour[a], Ganesh Raghavendran[b], Oleg Borodin[e], Minghao Zhang[b,*], Ying Shirley Meng[b,d,**]

[a] Materials Science and Engineering, University of California San Diego, La Jolla, CA 92093, USA
[b] Department of NanoEngineering, University of California San Diego, La Jolla, CA 92093, USA
[c] Center for Advanced Research and Computing, University of Southern California, Los Angeles, CA 90007, USA
[d] Pritzker School of Molecular Engineering, University of Chicago, Chicago, IL, 60637, USA
[e] Battery Science Branch, Energy Science Division, Army Research Directorate, DEVCOM Army Research Laboratory, Adelphi, MD 20783, USA

ARTICLE INFO

Keywords:
Li-ion batteries
Co-free cathode
All-fluorinated electrolyte
High temperature operation
Deprotonation reaction

ABSTRACT

Severe capacity degradation at high operating voltages and poor interphase stability at elevated temperature have thus far precluded the practical application of $LiNi_{0.5}Mn_{1.5}O_4$ (LNMO) as a cathode material for lithium-ion batteries. Addressing these challenges through a combination of experimental and theoretical methods in this work, we demonstrate how a fluorinated carbonate electrolyte enables both high-voltage and high temperature operation by mitigating the traditional interfacial reactions observed in electrolytes with conventional carbonate solvents. Computational studies confirm the exceptional oxidation stability of fluorinated carbonate electrolyte which reduces deprotonation at high voltage. The mitigated deprotonation will then minimize the formation of HF acid which corrodes the LNMO surface and leads to phase transformation and poor interphases. With fluorinated carbonate electrolyte at elevated temperature, it was found on LNMO's subsurface a reduced amount of Mn_3O_4 phase which can block Li^+ transfer and result in drastic cell failure. Leveraging this approach, LNMO/graphite full cells with a high loading of 3.0 mAh/cm^2 achieve excellent cycling stability, retaining ~84 % of their initial capacity at room temperature (25 °C) after 200 cycles and ~68 % after 100 cycles at 55 °C. This advanced electrolyte also shows promise for improving calendar life, retaining > 30 % more capacity than the carbonate baseline after high temperature storage. These results indicate that electrolytes based on fluorinated carbonates are a promising strategy for overcoming the remaining challenges toward practical commercial application of LNMO.

1. Introduction

Driven by demands for more sustainable and energy dense lithium-ion batteries (LIBs), researchers and technologists continue to pursue new battery chemistries with reduced dependence on critical minerals and which may offer exciting new capabilities [1]. $LiNi_{0.5}Mn_{1.5}O_4$ (LNMO) spinel is a high voltage cathode of particular interest, as it is an energy-dense, cobalt-free chemistry with reduced nickel content compared to commercialized layered cathodes. LNMO's ~20 % higher operating voltage (~4.7 V vs. 3.8 V for $LiNi_xCo_yMn_{1-x-y}O_2$ (NCM)) also provides a promising opportunity for high power density applications and flexibility in battery pack design. Unfortunately, LNMO's practical usage is still severely limited by parasitic reactions associated with its extremely oxidative operating conditions [2,3], including electrolyte decomposition and transition metal (TM) dissolution, which are further exacerbated under storage or operation at elevated temperature [4]. The limited progress that has been made toward addressing electrolyte decomposition issues and improving the performance of LNMO at elevated temperatures has in many cases been studied with LNMO half cells, which provides excess lithium, introduces compounding design challenges for stabilizing both Li metal and a high voltage cathode, and convolutes the mechanistic understanding of where parasitic reactions may be occurring in the cell [5–7].

For LNMO/graphite full cells which are likely more practical in the near future, electrolyte modifications such as novel additives and solvents

* Corresponding author.
** Corresponding author at: Department of NanoEngineering, University of California San Diego, La Jolla, CA 92093, USA.
E-mail addresses: miz016@ucsd.edu (M. Zhang), shirleymeng@uchicago.edu (Y.S. Meng).
[1] Weiliang Yao, Yixuan Li and Marco Olguin contributed equally to this work.

https://doi.org/10.1016/j.nxener.2024.100136
Received 2 January 2024; Received in revised form 8 April 2024; Accepted 29 April 2024

are still the most popular strategy. In one example, the use of Tris(trimethylsilyl) Phosphite (TMSPi), lithium difluoro(oxalato)borate (LiDFOB) and lithium difluorophosphate (LiDFP) in conventional ethylene carbonate (EC), diethyl carbonate (DEC) and dimethyl carbonate (DMC) effectively mitigated side reactions at the LNMO surface and formed a more robust cathode electrolyte interphase (CEI) [8,9]. However, the question remains whether conventional carbonate solvents with low oxidative stability can survive under both high voltage and high temperatures. Replacement of conventional carbonate-based solvents was also explored for high-voltage systems including the utilization of sulfone-based solvents [10] and ionic liquid [11]. Those solvents are carbonate-free and generally have very high oxidative stability. However, the practical implementation of these electrolytes is challenging due to their high viscosity and poor wettability, introducing challenges particularly for applications with thick electrodes. In our previous work, we also explained that LNMO needs to achieve at least 3 mAh/cm^2 ($> 90\ \mu$m) and > 90 % active materials composition to reach commercial viability [12]. Other than electrolyte modifications, surface modifications such as atomic layer deposition (ALD) coating of MgF_2 and TiO_2 [13,14] were also studied for protecting the LNMO surface under high voltage and to reduce TM dissolution. Nevertheless, the cost and equipment required for scaling up ALD processes is much less attractive than electrolyte engineering with respect to high-throughput manufacturing [15,16].

Recently, improved cycling stability using fluoroethylene carbonate (FEC) and methyl (2,2,2-trifluoroethyl) carbonate (FEMC) was demonstrated with other high-voltage cathode materials such as $LiCoPO_4$ (up to 5 V) [17], NCM523 (up to 4.6 V) [18,19], NCM622 (up to 4.5 V) [20] and NCM811 (up to 4.4 V) [21]. As the first to explore these two fluorinated solvents in LNMO/graphite system, Hu *et. al* used a combination of FEC, FEMC, and a fluorinated ether (F-EPE) in 2013 [22]. Their study concluded that reduced solid decomposition products deposited on both the anode and the cathode were the key to enable full cell cycling at both room temperature and 55 °C. However, the cost, potential environmental hazards, and toxicity to human health associated with many of these fluorinated ethers limit the practicality of this approach [23]. This demonstration along with a few subsequent publications with similar electrolyte formulations achieved additional progress, however, they generally lacked a mechanistic understanding of LNMO/graphite system at elevated temperature (**Figure S1**). One approach used $Li_4Ti_5O_{12}$ (LTO) as an anode to construct full cells [24]; however, the overall cell energy density was not comparable with LNMO/graphite due to the lower capacity and higher potential of LTO (~175 mAh/g). Another study by Zhou et al. used a combination of metal–organic-framework (MOF) separator and LiTFSI/Pyr_{13}TFSI-based ironic liquid electrolyte in LNMO/graphite full cells and achieved an astonishing 83.3 % capacity retention after 1000 cycles at 55 °C [25]. Nevertheless, the complex fabrication process of MOF separator and poor viscosity of ionic liquid electrolyte limit the applicability of this separator-electrolyte combination, and the LNMO loading in this work was only ~2.1 mg/cm^2, which is far from practical targets. Up to this point, the prevailing explanations for poor LNMO full cell performance were TM (especially Mn) dissolution and unstable interphases. While it is true that dissolved Mn ions from Mn-rich cathode such as LNMO and lithium manganese oxide (LMO) will be reduced on the graphite anode surface by depleting active Li^+ [26], the impact and root cause of TM dissolution on the cathode is not as well-defined.

As mentioned above, the high sensitivity of LIBs' performance to temperature will significantly limit the large-scale applications of LNMO. To obtain the optimum performance, the operating temperature of LIBs needs to be kept within a narrow range (15–35 °C) [27]. Operation at improper temperature range will bring about drastic performance degradation (e.g. capacity and power decay) and may even cause thermal runaway of LIBs. Therefore, a battery thermal management system (BTMS) that comprises cooler, heater, heat exchanger, sensors, pipelines, and pumps/fans is required when the battery pack is assembled [28,29]. The installation of complicated BTMS will unavoidably increase the weight and space of battery pack, thus significantly reduce the energy density and increase the overall cost. To reduce the reliance of BTMS, improving the temperature tolerance of LIBs is an effective approach to enhancing battery stability, safety, and utilization efficiency. In this work, combining experimental and computational approaches, we pinpoint the underlying mechanism of LNMO degradation with conventional carbonate electrolyte at 55 °C. We propose that the benefit of fluorinated carbonate electrolyte comes from the reduced deprotonation of fluorinated solvent molecules at high voltage and high temperature. This will in turn reduce free protons (H^+) that actively attack the LNMO's surface and form moisture (H_2O), which later hydrolyze $LiPF_6$ salt to form strong hydrofluoric (HF) acid. Loss of TM triggered by HF acid will lead to subsurface phase transformation from LNMO to Mn_3O_4 which ultimately blocks the Li^+ transfer from the bulk, therefore resulting in drastic impedance rise and cell failure. In addition, defluorination of FEC will help to form LiF to protect the LNMO surface from further HF attacks. With the improved oxidation and thermal stability of fluorinated carbonate electrolyte

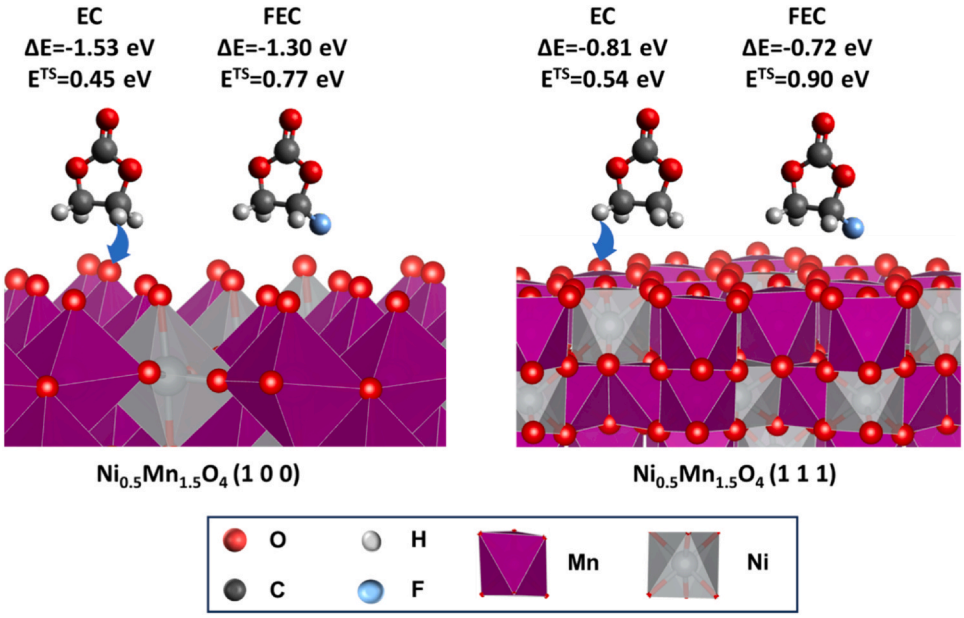

Fig. 1. Reactivity of EC and FEC solvents at the fully charged $Ni_{0.5}Mn_{1.5}O_4$ (NMO) surface from DFT calculations. ΔE and E^{TS} represent the reaction energy and reaction barrier, respectively.

(1 m $LiPF_6$ in FEC:FEMC = 3:7 wt/wt), LNMO/graphite full cells at practical loadings (3.0 mAh/cm^2 level) cycled at C/3 rate can achieve 68 % capacity retention after 100 cycles under 55 ˚C.

2. Results & discussion

2.1. Theoretical calculations and electrochemical evaluation of fluorinated electrolytes

It is well established that the high voltage LNMO cathode, in combination with carbonate-based electrolytes, undergoes a massive increase in parasitic reactivity upon cycling above 4.5 V vs Li. The increased electrolyte decomposition at a high state-of-charge deteriorates the long-term cycling performance and promotes self-discharge, ultimately leading to rapid battery failure. This accelerated electrolyte decomposition at operating voltages above 4.5 V serves as a major motivation for our adopting a fully de-lithiated cathode model. In using a fully de-lithiated $Ni_{0.5}Mn_{1.5}O_4$ slab (Fig. 1), we are probing the electrolyte/cathode interface under the most aggressive oxidative electrochemical environment for the electrolyte solvent. By performing nudged elastic band (NEB) calculations for low barrier electrolyte deprotonation reactions, we seek to gain insight into the initial stages of electrolyte decomposition at the high-voltage cathode interface. The calculated NEB reaction barriers and reaction energies are given in Fig. 1 for the two different electrolyte molecules (EC and FEC) interacting with the fully de-lithiated (111) and (100) facets of the disordered (Fd-3 m phase) spinel. Notably, the energy barriers are slightly larger for the (111) facet. EC exhibits the lower energy barrier on both surfaces whereas its fluorinated counterpart, FEC, shows the higher barrier, which can effectively slow down the electrolyte decomposition process.

After calculating the reaction barrier for deprotonation of FEC and EC, the effect was initially investigated in LNMO/graphite full cells at ~25 ˚C (room temperature). These full cells were assembled following the protocol developed in our previous work and the results are shown in Figs. 2a and b [12]. By replacing EC with FEC, after 200 cycles, the capacity retention of the full cell improved from 69.9 % to 74.7 %, while the average Coulombic efficiency (CE %) increased from 99.52 % to 99.68 %. These results strongly support the notion that based on the higher deprotonation reaction barrier, the more oxidatively stable FEC is less prone to side reactions on the LNMO surface and improves reversibility. Following the same concept of fluorination we obtained above, replacing EMC with FEMC in the full cell further improved the capacity retention to 84.4 %, with an average CE % of 99.75 %. It was also found in the literature that both FEC and FEMC were less favorable for deprotonation than EC on the fully charged $CoPO_4$ (010) surface (at 5 V) [17]. Moreover, by introducing $-CF_3$ into the structure, which is a strong electron-withdrawing group, many calculations show that fluorination of linear ethyl methyl carbonate (EMC) solvent molecules can significantly lower the highest occupied molecular orbital (HOMOs), thus improving the oxidative stability at high voltage [30–32]. Therefore, we attribute the significant (~15 %) increase in capacity retention of full cells at 25 ˚C to the oxidative stability improvements through fluorination of conventional carbonate solvent molecules. Indeed, it should not be ignored that the coin cell case corrosion at high voltage could be another factor that affects the coulombic efficiency [12]. Elevated temperature testing was also carried out to investigate and simulate the performance of LNMO/graphite system under practical conditions in real life (e.g. extremely hot weather in certain regions). In the high temperature cycling investigations (Figs. 2c and d), it was found that LNMO/graphite full cells at a practical 3 mAh/cm^2 level can still deliver a ~68 % capacity retention and 99.44 % average CE % after 100 cycles (**Figure S1**). In contrast, full cells using conventional EC-EMC electrolyte showed severe capacity and CE % fluctuations along cycling and finally failed after 70 cycles. A detailed diagnosis of both cathode and anode interfacial reactions/products is discussed in the next section.

High temperature storage testing was also conducted to evaluate the calendar life of LNMO/graphite full cell with both electrolytes. The cells were first cycled at C/10 rate for one cycle followed by two cycles at C/3 rate at ~25 ˚C. The cells were then stored and rested under 55 ˚C for 24 hours. After storage, the cells underwent one cycle at C/3 rate. As seen in **Figure S2**, full cells using FEC-FEMC after each one-day storage period can still recover most of the capacity with small error range. Full cells using EC-EMC, however, show similar capacity fluctuation trend as the cycling. This suggests that high oxidation stability is crucial to calendar life of high voltage cathode since the cells stay at high voltage during storage, leading to continuous decomposition of electrolyte. Particularly, LNMO's long plateaus of Ni^{4+} to Ni^{3+} and Ni^{3+} to Ni^{2+} at ~4.7 V requires the cells to remain at high voltage for longer periods

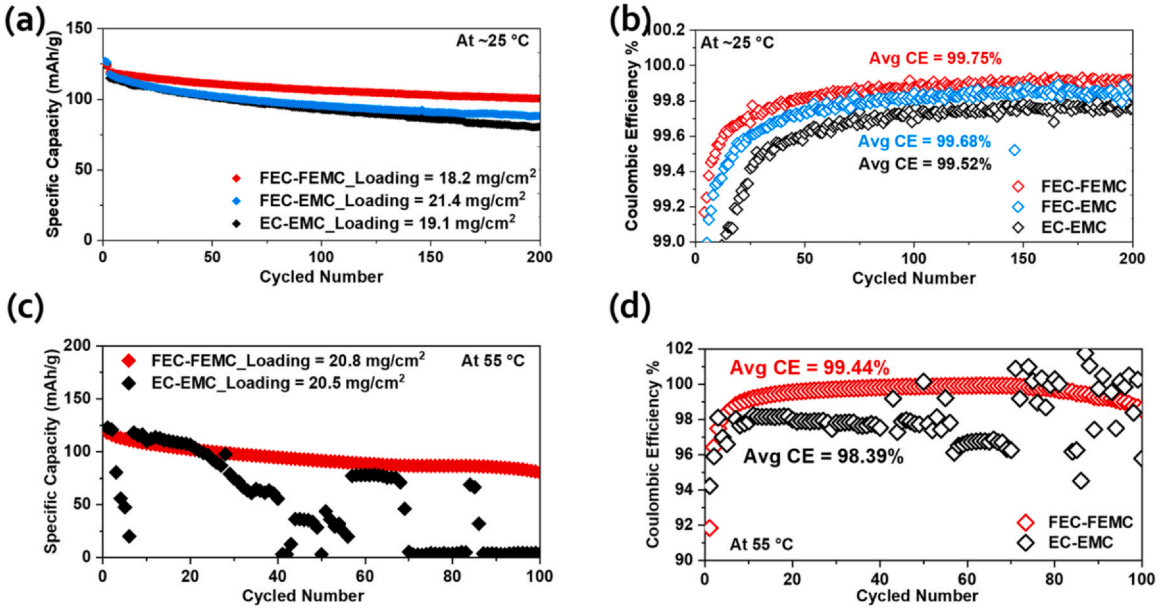

Fig. 2. Electrochemical performance of LNMO/graphite full cells under different conditions. (a) and (b) Long-term cycling of various electrolyte formulations at ~25 ˚C (room temperature), (c) and (d) cycling performance at an elevated temperature of 55 ˚C.

compared to conventional layer oxide materials such as NCM and lithium nickel cobalt aluminum oxide (NCA).

Other than electrochemical performance, safety and thermal stability are key parameters of interest in electrolyte development [33]. Herein, we perform differential scanning calorimetry (DSC) to examine the reactivity of LNMO/graphite with two types of electrolytes after fully charged at C/10 rate (**Figure S3**). As shown in **Figure S4**, no exothermic peak is observed, with all the peaks corresponding to solvent evaporation and separator melting. This implies that the LNMO/graphite system is relatively safe compared to LNMO/Li metal system with both electrolytes at the fully charged state. In addition, since LNMO does not exhibit oxygen release during charge/discharge process, the absence of oxygen further reduces the risk of catastrophic heat generation during operation [34,35]. Besides the electrochemical benefits contributed by FEC-FEMC formulation under high temperature, another advantage is the non-flammability, which is highly

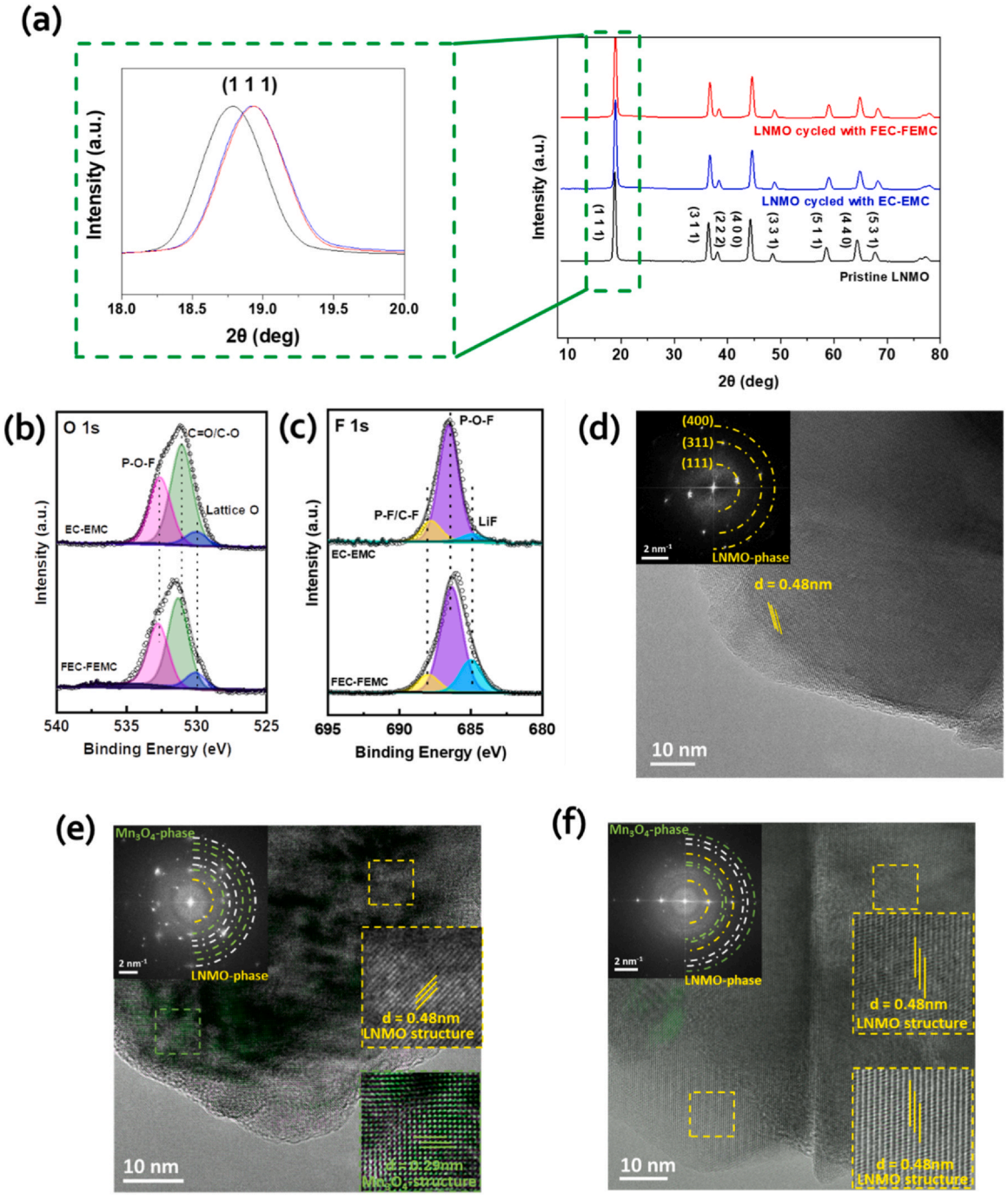

Fig. 3. (a) XRD results of cycled LNMO using baseline and fluorinated carbonate electrolyte at 55 ℃. XPS spectra of (b) O 1 s, (c) F 1 s of the cycled LNMO using different types of electrolytes. HRTEM and corresponding FFT patterns of (d) pristine LNMO and cycled LNMO in (e) EC-EMC and (f) FEC-FEMC electrolyte. The green semicircles in (e) indicate the lattice planes of (31 − 1), (60 − 1) and (222) of Mn_3O_4 structure from inner to outer, respectively. The yellow semicircle in (e) indicates the lattice plane of (111) of LNMO structure. The green semicircles in (f) indicate the lattice planes of (31 − 1), (40 − 1) and (60 − 1) of Mn_3O_4 structure from inner to outer, respectively. The yellow semicircles in (f) indicate the lattice planes of (111) and (222) of LNMO structure from inner to outer. respectively. The white circles indicate the lattice planes can belong to both phases. The IFFT images were created using the diffraction peaks from Mn_3O_4 structure and overlayed with the HRTEM images in (e) and (f).

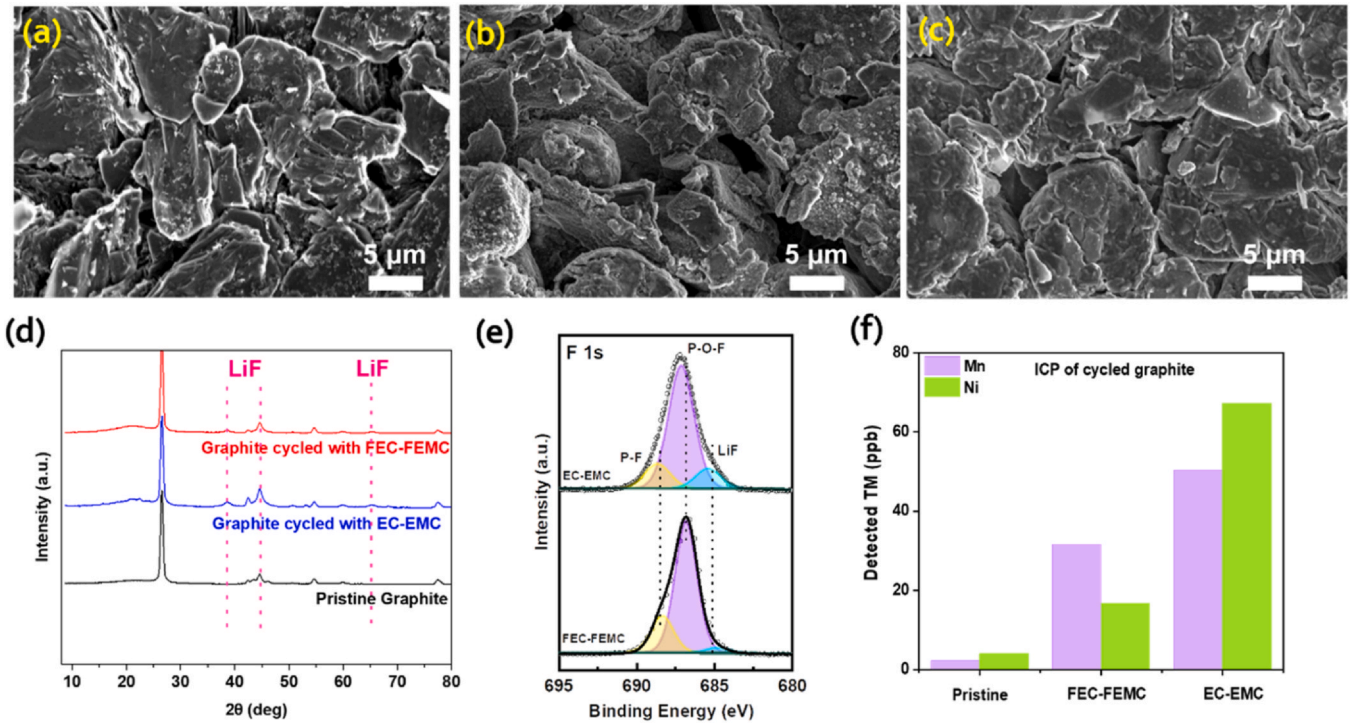

Fig. 4. Post-mortem analysis of graphite anode after cycling at 55 °C. SEM images of graphite electrode (a) at pristine state, cycled using (b) EC-EMC base and (c) FEC-FEMC base electrolyte. (d) Capillary X-ray diffraction, (e) XPS F 1 s spectra of cycled graphite anode using different types of electrolytes and (f) ICP-MS results showing transition metal (TM) dissolution and redeposition on the graphite anode.

desirable but is rarely a characteristic of non-aqueous electrolytes. As demonstrated in flame exposure tests (**Supplementary Videos 1** and **2**), glass fiber soaked in FEC-FEMC electrolyte does not burn following ignition, in sharp contrast with the highly flammable EC-EMC electrolyte. This can be explained by the fluorine substitution in FEMC effectively inhibiting the propagation of oxygen radicals during combustion [17].

Supplementary material related to this article can be found online at doi:10.1016/j.nxener.2024.100136.

2.2. Surface and bulk analysis of cycled LNMO and graphite electrode under 55 ˚C

To better understand the impact of interphase and bulk properties, both cathode and anode electrodes were collected after 100 cycles at 55 ˚C for characterization. Capillary X-ray diffraction (XRD) was first performed on the cycled LNMO electrodes. As shown in Fig. 3a, no additional peak was found, but the significant (1 1 1) peak shift of cycled LNMO indicates the loss of lithium inventory in the bulk structure. Even though the capacity difference between full cells using EC-EMC and FEC-FEMC is obvious (~0 % vs 68 %), the right shift of the (1 1 1) peak is consistently observed in both cathodes. Noting that the loss of Li in bulk structure is only part of the lithium inventory loss in the full cell, the major lithium inventory loss at the cathode side does not seem to occur in the bulk structure, but rather in the region close to the surface of LNMO. The interphase chemistry was then characterized using X-ray photoelectron spectroscopy (XPS). From the O 1 s spectra (Fig. 3b), the intensity of lattice oxygen peak (~530.0 eV) in the LNMO cycled in both electrolytes is similar. The F 1 s spectra in Fig. 3c also clearly indicates that the LNMO cycled in FEC-FEMC electrolyte has a LiF-rich CEI layer. The high-resolution transmission electron microscopy (HRTEM) results reveal that the surface of LNMO cycled with baseline EC-EMC electrolyte has a “broken” CEI shape while LNMO using FEC-FEMC maintains a thin and conformal 1–2 nm CEI (**Figure S5**). The “broken” CEI from LNMO cycled with EC-EMC consists of two large bumps while certain regions do not have CEI at all. Other CEI regions show similar thickness to the conformal CEI in LNMO cycled with FEC-FEMC. Notably different CEI properties in LNMO cycled with EC-EMC could be attributed to more significant attacks by the HF acid [36], triggered by the EC-EMC’s drastic decomposition under aggressive cycling conditions. Both EC and EMC will undergo deprotonation to regenerate free protons that can continuously attack the cathode’s surface to generate H_2O [37]. The deprotonation will exacerbate with the temperature rising. The trace amount of H_2O from the electrolyte and from the EC-EMC decomposition will react with PF_5, which is the major $LiPF_6$ salt decomposition product, to form strongly acidic HF which will further corrode the CEI. On the other hand, FEC and FEMC, which are more oxidatively stable, are less prone to decomposition under high voltage and high temperature, therefore leading to a more conformal CEI layer. However, the CEI layer only has a thickness in nanometer scale (< 20 nm even in EC-EMC’s poor CEI). It is unlikely this difference in the CEI layer can independently explain the sharp contrast of the high temperature cycling performance. Therefore, we further analyzed the HRTEM results of the LNMO subsurface, finding that the LNMO cycled with EC-EMC shows a significant subsurface structure change from LNMO phase to Mn_3O_4 phase. Since both LNMO and Mn_3O_4 have spinel structure, the subsurface phase change is identified by the change of d-spacing found in HRTEM results (**Table S1** and **S2**). The LNMO to Mn_3O_4 phase change is also previously reported in literature, suggesting that transition metal (TM) ions migrate into tetrahedral Li sites to form a Mn_3O_4-like structure [38]. In our case, it is possible that the HF acid attacks the bare LNMO region without CEI protection and corrodes the subsurface, leading to TM dissolution followed by TM migration to both tetrahedral Li sites. The formation of Mn_3O_4 likely blocks the Li^+ transfer and increases cell impedance, presenting a reasonable explanation for the capacity fluctuations followed by cell failure observed in Fig. 2c. Since this structural corrosion only occurs down to the subsurface, the inner bulk region is not affected, as shown in the XRD analysis. As discussed above, LNMO cycled in FEC-FEMC has a LiF-rich CEI layer. FEC is known to undergo de-

fluorination and decomposition to form LiF [39–41], which can also effectively protect the surface of LNMO. From backscattered electron scanning electron microscopy (BSE-SEM) images (**Figure S6(c), S6(e)**) and energy dispersive X-ray spectroscopy (EDX) results of LNMO electrodes (**Figure S7, Table S3** and **S4**), we can observe abundant LiF nanoparticles covering most of the LNMO surface. Since the LiF peak is not observable in the XRD results, the LiF layer is expected to be thin, passivating the LNMO surface and preventing further subsurface structural change.

To reveal a better understanding of the electrolyte's impact on the graphite anode, SEM was performed to observe the morphology of cycled graphite collected from full cells cycled with EC-EMC and FEC-FEMC (Figs. 4a-c). The SEM images show that that a bulky layer of the SEI is formed on the surface of graphite cycled in EC-EMC electrolyte. The results could suggest that severe parasitic reactions had occurred at the graphite anode which leads to accumulation of side reaction product on the surface. Interestingly, the surface of graphite cycled with FEC-FEMC still exhibits a relatively clean surface similar to pristine graphite. However, under BSE mode, unlike the nanoparticles which can be observed clearly on LNMO's surface, thick layer and large chunk of particles can be seen on the graphite surface (**Figure S8**). Combining the EDS results (**Figure S9**), the thick layers on both cycled graphite anodes are F-rich. Capillary XRD and XPS F 1 s spectra of graphite shown in Figs. 4d and e respectively pointed out that the side reaction products on graphite surface are LiF, P-O-F and P-F rich. LiF is well-known as the decomposition product of the $LiPF_6$ salt [42]. Unlike the cathode, the obvious LiF peaks appeared in XRD results in both graphite electrode samples also implies that large amount of LiF was formed on the graphite surface since the XRD is a bulk characterization technique. This F-rich thick layer could block the Li^+ intercalation/de-intercalation to the graphite layer and lead to further capacity loss under high temperatures. Under both high voltage and temperature, the solvation structure of PF_6-EC-EMC clearly cannot be maintained. To investigate the extent of transition metal dissolution and crosstalk, the inductively coupled plasma mass spectrometry (ICP-MS) results of cycled graphite anodes revealed more severe transition metal dissolution from cathode on graphite using EC-EMC electrolyte as shown in Fig. 4f. Pristine graphite is found to have Ni/Mn with < 5 ppb, which suggests a high purity graphite after purification process is used in this work [43]. Interestingly, despite the fact that LNMO is a Mn-rich cathode material, the dissolution of Ni after cycling is more prevalent than Mn. This finding is also consistent with EDX results (**Figure S10** and **Table S7** to **S8**), where Ni and F signals are much stronger on the surface of graphite cycled with EC-EMC. Considering the observed subsurface phase transition from LNMO to Mn_3O_4, larger amounts of Ni dissolution provide strong correlative evidence of the formation of Mn_3O_4.

2.3. Electrolyte analysis before and after storage under 55 °C

In addition to the interface and bulk investigations, characterizations of electrolyte before and after high temperature storage were also performed. Electrochemical Impedance Spectroscopy (EIS) of LNMO/LNMO symmetric cells using pristine and aged electrolytes was carried out to observe the impedance change caused by high temperature storage (**Figure S11**). In the EIS fitting, R_s represents electrolyte and ohmic resistance between working and reference electrodes, R_{ct} represents charge transfer resistance; Q represents double-layer capacitance of electrode/electrolyte interface, and W represents semi-infinite Warburg impedance associated with mass transport resistance. Both electrolytes experienced impedance increases after high temperature storage, but the overall resistance after aging is similar. Ionic conductivity and Fourier-transform infrared spectroscopy (FTIR) were performed to further understand the bulk electrolytes' differences brought by high temperature storage (**Figure S12** to **Figure S14**). Consistent with the FTIR data, ionic conductivity of both electrolytes shows marginal changes after aging at 55 °C, indicating negligible changes in the bulk electrolyte. However, when LNMO powder or electrodes were introduced into the electrolyte during storage, significant TM dissolution can be observed even though no electrochemical charge/discharge was involved (**Figure S15**). It can be seen from the pH testing results that the pH values of both electrolytes before storage are close to 6 while after storage, both electrolytes become extremely acidic (**Figure S16**). This could be due to the hydrolysis of the $LiPF_6$ salt since trace amount of water is always present in the pristine electrolytes. The hydrolysis process of $LiPF_6$ can be described by equations below [44]:

1) $LiPF_6 \rightleftharpoons LiF + PF_5$
2) $PF_5 + H_2O \rightarrow HF + POF_3$
3) $POF_3 + H_2O \rightarrow HF + HPO_2F_2$ (Further hydrolysis)
4) $HPO_2F_2 \rightarrow H+ + PO_2F_2^-$

During storage under high temperature, the hydrolysis of salt will be accelerated and leads to large amount of HF formation which will

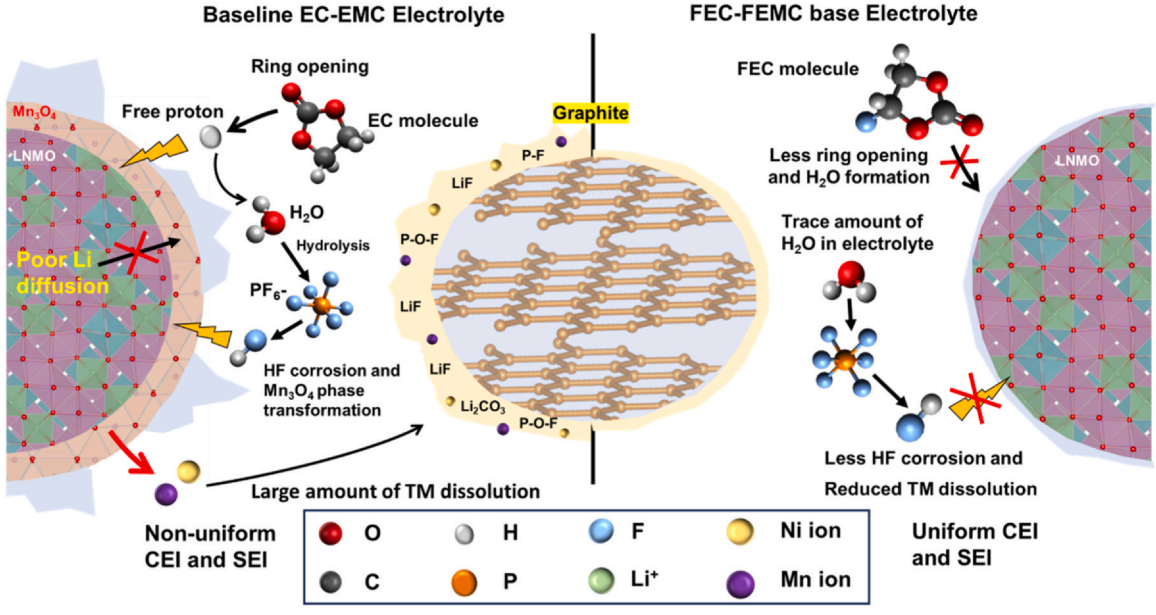

Fig. 5. Schematic of proposed degradation mechanism of EC-EMC base and FEC-FEMC base electrolyte on the LNMO surface.

actively attack the surface of LNMO. Therefore, significant TM dissolution from both LNMO powder and electrodes is observed in both electrolytes. The higher amount of TM dissolution in powder is possibly due to the larger contact area in LNMO powder compared to LNMO electrodes (some LNMO surface could be covered by PVDF and carbon). The much less TM dissolution found in FEC-FEMC electrolyte shows that the stability of $LiPF_6$ salt is much higher in the FEC-FEMC system possibly due to a different solvation structure. Combining the results above, bulk electrolyte will experience less changes during high temperature storage. However, when active materials are introduced, the electrolyte/electrode interphase evolution should be the limiting factor during long-term high temperature/voltage cycling and storage of LNMO/graphite full cells. The FEC-FEMC electrolyte not only demonstrates much improved oxidation stability (during charging/discharging at high voltage), but it also helps with stabilization of the $LiPF_6$ salt under high temperature, therefore mitigating the structural damage by reducing the HF formation from both salt hydrolysis and solvent decomposition.

The pronounced high temperature cycling found in LNMO/graphite full cells using FEC-FEMC electrolyte is ascribed to the combined factors of high oxidative stability of fluorinated solvent molecules and limited corrosion of the cathode surface. As illustrated in Fig. 5, baseline EC molecules undergo ring opening and generation of free protons during high voltage charging. These free protons will attack LNMO surface and generate more H_2O, which later hydrolyzes the $LiPF_6$ salt or PF_5 to form strong HF acid. The HF acid will then start to corrode both CEI and LNMO's bare surface to cause TM dissolution and Mn_3O_4 phase change. The Mn_3O_4 formed on LNMO subsurface will block the inner bulk Li^+ from shuttling to graphite anode, leading to impedance rising and severe capacity decay. The decomposed $LiPF_6$ salt will then be deposited on graphite surface to form a thick LiF-rich SEI, which prevents the Li^+ insertion. In contrast, when both EC and EMC solvent molecules are fluorinated, decomposition reaction barrier of FEC and FEMC molecules becomes higher, and the parasitic reactions are now less favorable under high voltage and are slowed down at high temperature. As a result, the chance of ring opening reactions found in EC are less likely to occur in FEC, therefore mitigating the following formation of HF acid. With less HF attack on LNMO surface, less TM dissolution is observed. As a result, the Mn_3O_4 phase transition on LNMO subsurface and TM deposition on the graphite are reduced and stable cycling is enabled in the full cell under high temperature.

To further test the ability of electrolytes under more harsh conditions such as potential Li dendritic growth, both electrolytes were tested in LNMO/Li metal full cells where 50 μm Li metal was used as the counter electrode (**Figure S17**). At ~25 °C, the full cells can last more than 100 cycles with > 90 % capacity retention and average CE % of 99.70 %. Even at 55 °C, the full cells can still last for 20 cycles. In contrast, Li metal full cells with EC-EMC electrolyte failed very quickly in several cycles after testing started. This is consistent with previous literature finding that neither EC nor EMC is compatible with Li metal anode [45,46]. Considering our previous findings highlighted the importance of stack pressure of Li metal full cells, the coin cell setup does not have any stack pressure control [47]. Hence, there is still large room for improvement in LNMO/Li metal full cells.

3. Conclusion

In this work, we proposed an electrolyte based on two fluorinated carbonates, 1 m $LiPF_6$ in FEC:FEMC = 3:7 wt/wt, to explore performance improvements of LNMO/graphite full cell cycling at ~25 °C (room temperature) and 55 °C. Combining both experimental and computational approaches, we demonstrate full cells with 3.0 mAh/cm^2 (~21 mg/cm^2 and ~90 μm) level loading to achieve ~84 % of their initial capacity at ~25 °C after 200 cycles and ~68 % after 100 cycles at 55 °C. The oxidatively stable FEC and FEMC solvents help mitigate LNMO subsurface structure change, TM dissolution, and Li inventory loss at the graphite anode. Looking forward, this FEC-FEMC electrolyte formulation has the potential to be modified with novel additives and high salt concentrations to further stabilized the $LiPF_6$ containing system through the elimination of the reactive substances (e.g. HF acid) generated in electrolyte decomposition processes. Moreover, the solvation structure of FEC-FEMC electrolyte is yet to be explored. A favorable solvation structure can enable more stable operation at high voltage and elevated temperature [48–51]. Last but not least, these findings may also be applied to other types of cathodes operating with voltages higher than 4.5 V (e.g., Li-rich layer oxide, $LiCoMnO_4$, olivine $LiCoPO_4$, high voltage $LiCO_2$ and NCM), etc., opening the door for the commercialization of high-voltage cathode materials.

Declaration of Competing Interest

The authors declare the following financial interests/personal relationships which may be considered as potential competing interests: Weiliang Yao reports financial support was provided by U.S. Department of Energy. If there are other authors, they declare that they have no known competing financial interests or personal relationships that could have appeared to influence the work reported in this paper.

Acknowledgements

This work was supported by the U.S. Department of Energy. Cathode material in this work was supported by the U.S. Department of Energy's Office of Energy Efficiency and Renewable Energy (EERE) and U.S. Army Tank & Automotive Research Development and Engineering Command (TARDEC) under the award number: DEEE0008442. M.A.S. and O.B. gratefully acknowledge support for this work by the US Department of the Army and the DEVCOM Army Research Laboratory. The SEM-EDX and HRTEM in this work were performed in part at the San Diego Nanotechnology Infrastructure (SDNI) of UCSD, a member of the National Nanotechnology Coordinated Infrastructure, which is supported by the National Science Foundation (Grant ECCS-1542148). The XPS in this work were performed at the UC Irvine Materials Research Institute (IMRI). The ICP-MS and XRD testing in this work were conducted at Environmental and Complex Analysis Laboratory (ECAL) in the Chemistry and Biochemistry department in UC San Diego. The authors thank Neware Instruments for the Neware battery test system. The authors thank Bingyu Lu for technical discussion. The authors thank Prof. Zhaoping Liu's group from Ningbo Institute of Materials Technology & Engineering (NIMTE) for providing the graphite anode.

Authors contribution

W.Y., M.Z., and Y.S.M. designed the experiments. M.O. and O.B. conducted the NEB calculations. M.A.S. performed electrolyte screening and provided electrolyte materials. W.Y. and Y.L. conducted electrode fabrication, electrochemistry testing, SEM-EDX and all data analysis. W.L. and W.Y. conducted XPS and ICP measurement. A.L. conducted the EIS and ionic conductivity test of electrolytes. N.P. conducted ICP measurement of the electrolyte in soaking test. S.B. conducted HRTEM experiments and analysis. B.S. conducted XRD experiment. B.B. conducted the DSC measurements. G.R. conducted flame testing and FTIR. W.Y. conducted XPS, XRD, SEM-EDX, DSC and ICP data analysis. Y.S.M. and M.Z. supervised the research. W.Y., M.Z. and M.A.S. wrote and edited the manuscript. All authors contributed to the discussion and provided feedback on the manuscript.

Additional information

All data is available in the main text or the supplementary materials. All data needed to evaluate the conclusions in the paper are present in the paper or the supplementary materials.

Appendix A. Supporting information

Supplementary data associated with this article can be found in the online version at doi:10.1016/j.nxener.2024.100136.

References

[1] B.S. Lee, Z. Wu, V. Petrova, X. Xing, H.D. Lim, H. Liu, P. Liu, J. Electrochem. Soc. 165 (3) (2018) A525–A533.
[2] T. Yoon, J. Soon, T.J. Lee, J.H. Ryu, S.M. Oh, J. Power Sources 503 (2021) 230051.
[3] H. Xu, H. Zhang, J. Ma, G. Xu, T. Dong, J. Chen, G. Cui, ACS Energy Lett. 4 (12) (2019) 2871–2886.
[4] J. Wang, Q. Zheng, M. Fang, S. Ko, Y. Yamada, A. Yamada, Adv. Sci. 8 (18) (2021) 2101646.
[5] C.T. Chu, A. Mondal, N.V. Kosova, J.Y. Lin, Appl. Surf. Sci. 530 (2020) 147169.
[6] Nguyen, M.T., Pham, H.Q., Berrocal, J.A., Gunkel, I. and Steiner, U. Journal of Materials Chemistry A, 11(14), pp.7670-7678.
[7] M. Li, Q. Li, M. Hu, Y. Du, Z. Duan, H. Fan, Y. Cui, S. Liu, Y. Jin, W. Liu, Phys. Chem. Chem. Phys. 24 (20) (2022) 12214–12225.
[8] A. Jamal, G.D. Salian, A. Mathew, W. Wahyudi, R.P. Carvalho, R. Gond, S.K. Heiskanen, D. Brandell, R. Younesi, ChemElectroChem 10 (16) (2023) e202300139.
[9] H. Chen, B. Liu, Y. Wang, H. Guan, H. Zhou, J. Alloy. Compd. 876 (2021) 159966.
[10] J. Alvarado, M.A. Schroeder, M. Zhang, O. Borodin, E. Gobrogge, M. Olguin, M.S. Ding, M. Gobet, S. Greenbaum, Y.S. Meng, K. Xu, Mater. Today 21 (4) (2018) 341–353.
[11] E.R. Østli, A. Mathew, J.R. Tolchard, D. Brandell, A.M. Svensson, S.M. Selbach, N.P. Wagner, Batter. Supercaps 6 (7) (2023) e202300085.
[12] W. Li, Y.G. Cho, W. Yao, Y. Li, A. Cronk, R. Shimizu, M.A. Schroeder, Y. Fu, F. Zou, V. Battaglia, A. Manthiram, M. Zhang, Y.S. Meng, J. Power Sources 473 (2020) 228579.
[13] A. Kraytsberg, H. Drezner, M. Auinat, A. Shapira, N. Solomatin, P. Axmann, M. Wohlfahrt-Mehrens, Y. Ein-Eli, ChemNanoMat 1 (8) (2015) 577–585.
[14] E.R. Østli, M. Ebadi, Y. Tesfamhret, M. Mahmoodinia, M.J. Lacey, D. Brandell, A.M. Svensson, S.M. Selbach, N.P. Wagner, ChemSusChem 15 (12) (2022) e202200324.
[15] U. Nisar, N. Muralidharan, R. Essehli, R. Amin, I. Belharouak, Energy Storage Mater. 38 (2021) 309–328.
[16] Liu, Y., Zhang, R., Wang, J. and Wang, Y. IScience, 24(4).
[17] X. Fan, L. Chen, O. Borodin, X. Ji, J. Chen, S. Hou, T. Deng, J. Zheng, C. Yang, S.C. Liou, K. Amine, K. Xu, C.S. Wang, Nat. Nanotechnol. 13 (8) (2018) 715–722.
[18] M. He, C.C. Su, Z. Feng, L. Zeng, T. Wu, M.J. Bedzyk, P. Fenter, Y. Wang, Z. Zhang, Adv. Energy Mater. 7 (15) (2017) 1700109.
[19] J. Yang, Q. Liu, K.Z. Pupek, T.L. Dzwiniel, N.L. Dietz Rago, J. Cao, N. Dandu, L. Curtiss, K. Liu, C. Liao, Z. Zhang, ACS Energy Lett. 6 (2) (2021) 371–378.
[20] G.J. Chung, J. Han, S.W. Song, ACS Appl. Mater. Interfaces 12 (38) (2020) 42868–42879.
[21] T. Yang, S. Li, W. Wang, J. Lu, W. Fan, X. Zuo, J. Nan, J. Power Sources 505 (2021) 230055.
[22] L. Hu, Z. Zhang, K. Amine, Electrochem. Commun. 35 (2013) 76–79.
[23] W.T. Tsai, J. Hazard. Mater. 119 (1-3) (2005) 69–78.
[24] B. Aktekin, M.J. Lacey, T. Nordh, R. Younesi, C. Tengstedt, W. Zipprich, D. Brandell, K. Edström, J. Phys. Chem. C 122 (21) (2018) 11234–11248.
[25] Y. Qiao, Y. He, K. Jiang, Y. Liu, X. Li, M. Jia, S. Guo, H. Zhou, Adv. Energy Mater. 8 (33) (2018) 1802322.
[26] N.P. Pieczonka, Z. Liu, P. Lu, K.L. Olson, J. Moote, B.R. Powell, J.H. Kim, J. Phys. Chem. C 117 (31) (2013) 15947–15957.
[27] H. Liu, Z. Wei, W. He, J. Zhao, Energy Convers. Manag. 150 (2017) 304–330.
[28] T.M. Bandhauer, S. Garimella, T.F. Fuller, J. Electrochem. Soc. 158 (3) (2011) R1.
[29] Q. Wang, B. Jiang, B. Li, Y. Yan, Renew. Sustain. Energy Rev. 64 (2016) 106–128.
[30] Y. Wang, Y. Zhang, S. Dong, W. Zhou, P.K. Lee, Z. Peng, C. Dang, P.H.L. Sit, J. Guo, D.Y. Yu, Adv. Energy Mater. 12 (19) (2022) 2103360.
[31] Z. Zhang, L. Hu, H. Wu, W. Weng, M. Koh, P.C. Redfern, L.A. Curtiss, K. Amine, Energy Environ. Sci. 6 (6) (2013) 1806–1810.
[32] Q. Zheng, Y. Yamada, R. Shang, S. Ko, Y.Y. Lee, K. Kim, E. Nakamura, A. Yamada, Nat. Energy 5 (4) (2020) 291–298.
[33] B. Lu, D. Cheng, B. Sreenarayanan, W. Li, B. Bhamwala, W. Bao, Y.S. Meng, ACS Energy Lett. 8 (7) (2023) 3230–3238.
[34] M. He, L. Boulet-Roblin, P. Borel, C. Tessier, P. Novák, C. Villevieille, E.J. Berg, J. Electrochem. Soc. 163 (2) (2015) A83.
[35] M. Barbara, S. Heino, B. Thomas, B. Torsten, J. Jürgen, Neutron Imaging, Press. Meas. (2016).
[36] S. Park, S.Y. Jeong, T.K. Lee, M.W. Park, H.Y. Lim, J. Sung, J. Cho, S.K. Kwak, S.Y. Hong, N.S. Choi, Nat. Commun. 12.1 (2021) 1–12.
[37] Y. Zhang, Y. Katayama, R. Tatara, L. Giordano, Y. Yu, D. Fraggedakis, J.G. Sun, F. Maglia, R. Jung, M.Z. Bazant, Y. Shao-Horn, Energy Environ. Sci. 13 (1) (2020) 183–199.
[38] M. Lin, L. Ben, Y. Sun, H. Wang, Z. Yang, L. Gu, X. Yu, X.Q. Yang, H. Zhao, R. Yu, M. Armand, X. Huang, Chem. Mater. 27 (1) (2015) 292–303.
[39] C. Xu, F. Lindgren, B. Philippe, M. Gorgoi, F. Bjorefors, K. Edstrom, T. Gustafsson, Chem. Mater. 27 (7) (2015) 2591–2599.
[40] Y. Wang, Y. Liu, Y. Tu, Q. Wang, J. Phys. Chem. C 124 (17) (2020) 9099–9108.
[41] T. Hou, G. Yang, N.N. Rajput, J. Self, S.W. Park, J. Nanda, K.A. Persson, Nano Energy 64 (2019) 103881.
[42] S. Kim, M. Kim, I. Choi, J.J. Kim, J. Power Sources 336 (2016) 316–324.
[43] W. Kiciński, S. Dyjak, Carbon 168 (2020) 748–845.
[44] D. Mroz, J. Hartwig, S. Neitzel-Grieshammer, ECS Adv. 2.3 (2023) 030506.
[45] F. Ding, W. Xu, X. Chen, J. Zhang, M.H. Engelhard, Y. Zhang, B.R. Johnson, J.V. Crum, T.A. Blake, X. Liu, J.G. Zhang, J. Electrochem. Soc. 160 (10) (2013) A1894.
[46] L.A. Huff, H. Tavassol, J.L. Esbenshade, W. Xing, Y.M. Chiang, A.A. Gewirth, ACS Appl. Mater. Interfaces 8 (1)) (2016) 371–380.
[47] B. Lu, W. Bao, W. Yao, J.M. Doux, C. Fang, Y.S. Meng, J. Electrochem. Soc. 169 (7) (2022) 070537.
[48] Y. Zou, Z. Ma, G. Liu, Q. Li, D. Yin, X. Shi, Z. Cao, Z. Tian, H. Kim, Y. Guo, C. Sun, L. Cavallo, L. Wang, H. Alshareef, Y. Sun, J. Ming, Angew. Chem. 135 (8) (2023) e202216189.
[49] Y. Zou, G. Liu, Y. Wang, Q. Li, Z. Ma, D. Yin, Y. Liang, Z. Cao, L. Cavallo, H. Kim, L. Wang, H. Alshareef, Y. Sun, J. Ming, Adv. Energy Mater. 13 (19) (2023) 2300443.
[50] H. Cheng, Q. Sun, L. Li, Y. Zou, Y. Wang, T. Cai, F. Zhao, G. Liu, Z. Ma, W. Wahyudi, Q. Li, J. Ming, ACS Energy Lett. 7 (1) (2022) 490–513.
[51] Y. Zou, Z. Cao, J. Zhang, W. Wahyudi, Y. Wu, G. Liu, Q. Li, H. Cheng, D. Zhang, G.T. Park, L. Cavallo, T. Anthopoulos, L. Wang, Y. Sun, J. Ming, Adv. Mater. 33 (43) (2021) 2102964.